

# UC San Diego

## UC San Diego Previously Published Works

### Title

Structural interplay of anesthetics and paralytics on muscle nicotinic receptors.

### Permalink

<https://escholarship.org/uc/item/6nd9j0br>

### Journal

Nature communications, 14(1)

### ISSN

2041-1723

### Authors

Goswami, Umang  
Rahman, Md Mahfuzur  
Teng, Jinfeng  
et al.

### Publication Date

2023-06-01

### DOI

10.1038/s41467-023-38827-5


Peer reviewed

# Structural interplay of anesthetics and paralytics on muscle nicotinic receptors

Received: 30 March 2023

Accepted: 17 May 2023

Published online: 01 June 2023

 Check for updatesUmang Goswami<sup>1</sup>, Md Mahfuzur Rahman<sup>1,3</sup>, Jinfeng Teng<sup>2</sup> & Ryan E. Hibbs<sup>1,2</sup> 

General anesthetics and neuromuscular blockers are used together during surgery to stabilize patients in an unconscious state. Anesthetics act mainly by potentiating inhibitory ion channels and inhibiting excitatory ion channels, with the net effect of dampening nervous system excitability. Neuromuscular blockers act by antagonizing nicotinic acetylcholine receptors at the motor endplate; these excitatory ligand-gated ion channels are also inhibited by general anesthetics. The mechanisms by which anesthetics and neuromuscular blockers inhibit nicotinic receptors are poorly understood but underlie safe and effective surgeries. Here we took a direct structural approach to define how a commonly used anesthetic and two neuromuscular blockers act on a muscle-type nicotinic receptor. We discover that the intravenous anesthetic etomidate binds at an intrasubunit site in the transmembrane domain and stabilizes a non-conducting, desensitized-like state of the channel. The depolarizing neuromuscular blocker succinylcholine also stabilizes a desensitized channel but does so through binding to the classical neurotransmitter site. Rocuronium binds in this same neurotransmitter site but locks the receptor in a resting, non-conducting state. Together, this study reveals a structural mechanism for how general anesthetics work on excitatory nicotinic receptors and further rationalizes clinical observations in how general anesthetics and neuromuscular blockers interact.

Nicotinic acetylcholine receptors on muscle fibers are inhibited by many general anesthetics and are the principal targets of neuromuscular blockers used in surgery<sup>1</sup>. General anesthetics act mainly by targeting ligand-gated ion channels in the nervous system including those of the Cys-loop receptor family<sup>2,3</sup>. Within this pentameric channel family, intravenous anesthetics such as etomidate potentiate inhibitory GABA<sub>A</sub> receptors and inhibit excitatory nicotinic acetylcholine receptors<sup>4,5</sup>. These combined actions lead to an overall reduction of neuronal activity<sup>5,6</sup>. Neuromuscular blockers, or paralytic agents, antagonize the muscle nicotinic acetylcholine receptor thereby disrupting signaling between motor neurons and skeletal muscle. They are used in combination with general anesthetics to enable muscle relaxation and to lower the amount of general anesthetic required

during surgery, which improves safety and hastens recovery<sup>7</sup>. General anesthetics themselves also inhibit the muscle-type nicotinic receptor<sup>4,8–11</sup>; isoflurane, for example, is known to increase the efficacy of the neuromuscular blocker succinylcholine<sup>12</sup>. How general anesthetics modulate the muscle-type nicotinic receptor and alter the activity of neuromuscular blockers remains poorly understood.

Neuromuscular blocking agents fall into two categories. Depolarizing blockers cause transient nicotinic receptor channel opening and muscle fasciculations before stabilizing a nonconducting, desensitized channel state. This prolonged desensitization results in skeletal muscle paralysis. Succinylcholine is the most commonly used drug in this category<sup>13,14</sup>. Non-depolarizing blockers like rocuronium do not cause channel opening but instead stabilize a distinct nonconducting

<sup>1</sup>Department of Neuroscience and O'Donnell Brain Institute, University of Texas Southwestern Medical Center, Dallas, TX 75390, USA. <sup>2</sup>Department of Neurobiology, University of California, San Diego, La Jolla, CA 92093, USA. <sup>3</sup>Present address: Thermo Fisher Scientific, Rockford, IL 61101, USA.

 e-mail: [rehibbs@ucsd.edu](mailto:rehibbs@ucsd.edu)

channel state resulting in paralysis. Both muscle relaxants directly compete with acetylcholine and thereby block its action at the muscle nicotinic receptor, and both are used for rapid onset of muscle paralysis and aid in endotracheal intubation. Direct structural insights into how these clinically useful neuromuscular blockers bind to and antagonize the muscle-type nicotinic receptor are absent.

Here we used cryo-electron microscopy (cryo-EM) and electrophysiology to understand how general anesthetics and neuromuscular blockers act at the muscle-type nicotinic receptor, and to provide a foundation for understanding drug interactions. We report four high-resolution cryo-EM structures of a muscle-type nicotinic receptor in complex with the general anesthetic etomidate and the agonist choline, with the depolarizing blocker succinylcholine, and in two distinct states bound to the non-depolarizing blocker rocuronium. We first define where etomidate binds and how its binding affects receptor conformation and activity. We then contrast the anesthetic and blocker bound structures of the receptor to reveal common and distinct mechanisms of inhibition. We use electrophysiology to relate observed structures to physiological states. Together, we discover a negative modulator binding site for etomidate and elucidate inhibition mechanisms potentially relevant to drug interactions in clinical anesthesia.

## Results

### Biochemistry and receptor architecture

We purified the muscle-type nicotinic acetylcholine receptor from the electric organ of *Torpedo californica* and reconstituted it into lipid nanodiscs for structure determination by cryo-EM<sup>15</sup>. This receptor has long served as a model system for the human muscle receptor<sup>16–20</sup>, and retains the relevant pharmacology for neuromuscular blockers and etomidate<sup>9,21–23</sup>. The receptor assembles as a pentamer from four homologous subunits arranged  $\alpha$ - $\gamma$ - $\alpha$ - $\delta$ - $\beta$  pseudo-symmetrically around the channel axis (Fig. 1 and Supplementary Fig. 1)<sup>24–26</sup>. The large extracellular domain (ECD) harbors the classical neurotransmitter binding sites at  $\alpha$ - $\gamma$  and  $\alpha$ - $\delta$  interfaces<sup>24</sup>. The transmembrane domain (TMD) of four  $\alpha$ -helices per subunit forms a pore lined by the M2 helices. The intracellular domain (ICD), which is partly disordered in all known structures, comprises extensions of the M4 helix that frame lateral portals for tuning ion conductance. We preformed complexes of the receptor with etomidate, succinylcholine, and rocuronium before freezing samples for electron microscopy. This approach enabled determination of structures to overall resolutions of 2.7–2.9 Å, with density quality sufficient for modeling ligands and all of the receptor ECD, TMD, and all of the predicted intracellular MX and MA helices (Fig. 1, Supplementary Table 1, Supplementary Figs. 1 and 2, Supplementary Movies 1–9).

### Etomidate acts through an intrasubunit TMD site

The general anesthetic etomidate inhibits the activity of the muscle-type nicotinic receptor at concentrations that occur during clinical anesthesia<sup>7,10,11,27</sup>. Photoaffinity labeling studies have suggested several potential etomidate binding sites<sup>23,27–30</sup>. We performed electrophysiology experiments to better understand which steps in the channel gating cycle etomidate stabilizes: resting, activated, or desensitized (Fig. 1a, b). We observed that etomidate reduced the peak agonist response and further found that etomidate increased the current decay rate upon agonist exposure (Fig. 1b). This increase in decay rate likely stems from enhancing desensitization at low concentrations coupled with channel block at higher etomidate concentrations as suggested by photoaffinity studies<sup>27,29</sup>. Together these results indicate that etomidate's inhibitory activity at concentrations used during anesthesia (EC<sub>50</sub> for anesthesia of 2–4  $\mu$ M<sup>7,10,28</sup>) may stem from stabilizing a nonconducting desensitized state, to which agonists bind most tightly. Notably, photoaffinity based studies found that during brief activation, etomidate principally acts by inhibiting the

activated state<sup>23</sup>, while at an equilibrium accessible more readily by structural biology, etomidate stabilizes a desensitized channel state<sup>27</sup>. To provide a structural framework for where etomidate binds, and how it inhibits the channel, we obtained a cryo-EM structure of the muscle-type nicotinic receptor bound to etomidate at 2.8 Å overall resolution (Fig. 1c–e, Supplementary Figs. 1 and 2, Supplementary Table 1).

The cryo-EM map revealed unambiguous density for etomidate within the transmembrane domain of each principal ( $\alpha$ ) subunit (Fig. 1c–e). This intrasubunit site came as a surprise as it is strikingly distinct from etomidate's site in the homologous GABA<sub>A</sub> receptor. In this related anion-selective channel, etomidate binds at  $\beta$ - $\alpha$  subunit interfaces and acts as a positive modulator (Fig. 1c, Supplementary Fig. 3)<sup>31</sup>. The muscle receptor binding site, in contrast, is formed by the extracellular ends of the  $\alpha$ -subunit M1, M3, and M4 helices. The accessibility of this site depends upon detachment of the M4 C-terminus from the receptor, which is observed at least partially in all agonist-bound structures of the muscle-type nicotinic receptor (Fig. 1c–e and Supplementary Fig. 4). Indeed, in previous work we determined that conformational transitions in this site contributed to recovery from desensitization<sup>20</sup>. The pose of etomidate is equivalent at both its  $\alpha$ -subunit binding sites, with its phenyl ring orienting toward the intracellular side of the membrane, the imidazole ring normal to the membrane and the ester group pointing toward the extracellular side (Fig. 1e). The phenyl ring of etomidate makes  $\pi$ -stacking and Van der Waals interactions with surrounding phenylalanine residues (M4-F414, M3-F284 and M3-F280). Etomidate further forms hydrophobic contacts with M4-I417, M4-C418, M1-F227 and M3-Y277. These amino acids are conserved among *Torpedo*, mouse, and human receptors. Only M4-I417 is substituted by valine in humans. The binding site conservation suggests that observations for etomidate effects through this site would translate to mammalian species including humans. Mutagenesis of binding site residues did not reveal large changes in etomidate inhibition, perhaps due to the flexible nature of the binding site and the lack of electrostatic interactions made by the drug (Supplementary Fig. 5). The  $\alpha$ -M4 helix was identified previously from photolabeling studies<sup>27</sup> to be a potential etomidate binding site (Supplementary Fig. 6). However, the labeled residues in M4 do not orient toward the observed drug binding pocket. Mismatches between results from electron microscopy and photolabeling may stem from the latter being able to highlight lower occupancy, lower affinity sites, and from the photoreactive etomidate derivatives binding differently from the unmodified compound. Additional density specific to the etomidate-bound structure was apparent but not modeled in the upper half of the pore and extending from M4-M415 and M4-C418 (Supplementary Fig. 7 and Supplementary Movie 10). The pore density, which was diffuse, is consistent with a low affinity pore block site for etomidate suggested by photoaffinity studies<sup>27</sup>. The density extending from the M4 cysteine, adjacent to bound etomidate, may arise from a lipid that becomes ordered when etomidate is bound, or from the *N*-ethylmaleimide treatment used to prevent disulfide crosslinking during purification.

We obtained the etomidate-bound receptor structure using a purification strategy previously optimized to determine the apo, resting state of the receptor<sup>20</sup>. However, the etomidate complex cryo-EM map revealed density consistent with the weak agonist choline positioned in the classical neurotransmitter binding pocket (Fig. 1f). A very high concentration of choline (1.2 M) was used to elute the receptor during affinity chromatography but was then omitted from subsequent size exclusion chromatography and is not seen in our apo receptor map. The structural results suggest that etomidate increases the affinity for agonists in the neurotransmitter binding pocket, observed in binding measurements<sup>27</sup>, so much so that choline stays bound to the receptor throughout the final steps of purification. Consistent with bound agonist, loop C packs down tightly on the subunit

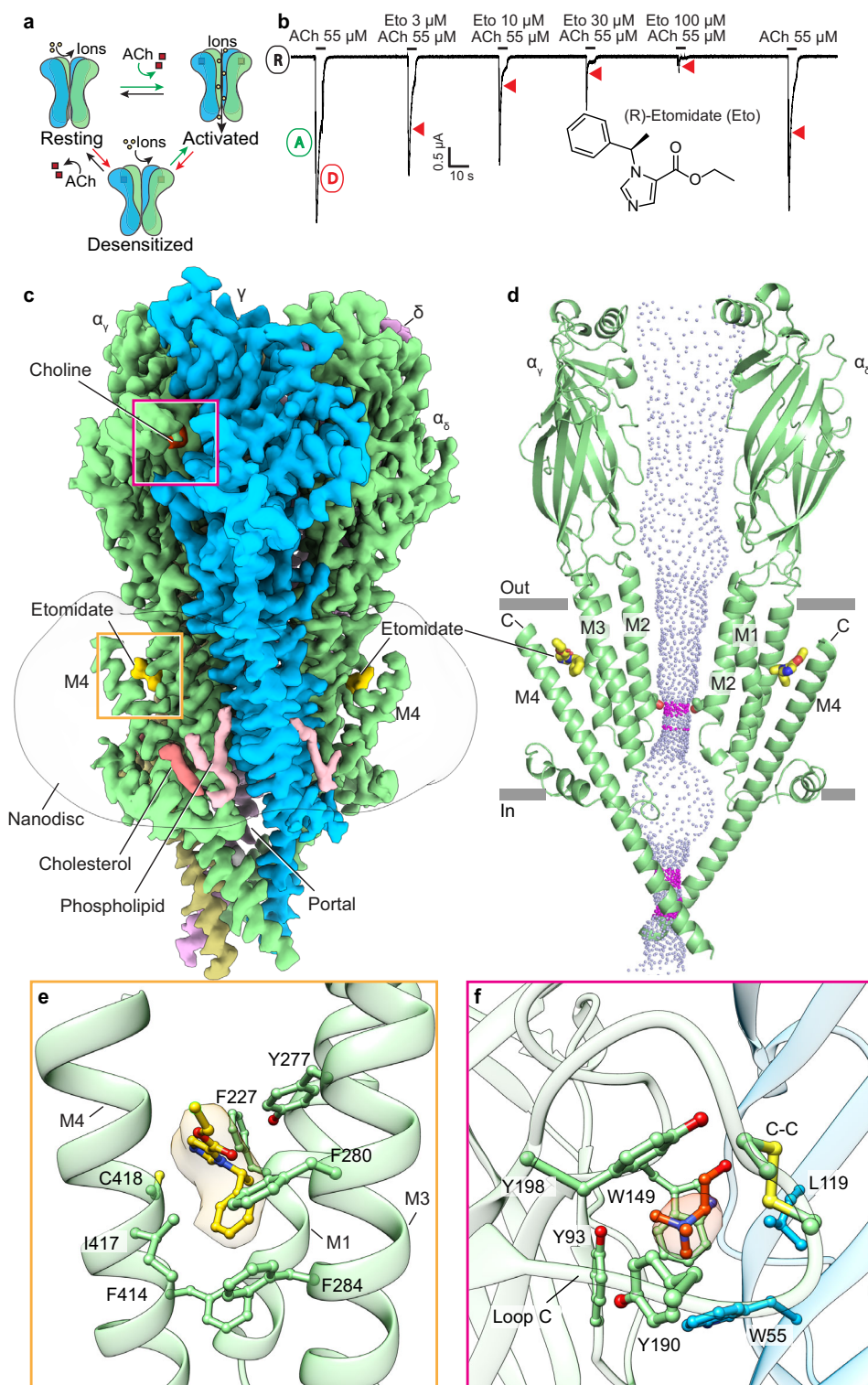


### Fig. 1 | Etomidate stabilizes a desensitized state through TMD binding.

**a** Simplified gating cycle cartoon for the nicotinic receptor. Acetylcholine (ACh) binding shifts the conformational equilibrium toward a conducting, activated state, then to the more stable nonconducting desensitized state. **b** Two-electrode voltage clamp (TEVC) electrophysiology shows activation by acetylcholine and dose-dependent receptor antagonism by etomidate (Eto). R, A, and D indicate channel resting state, and activation and presumed desensitization components of current response. Red triangles highlight etomidate increasing apparent desensitization rate. Incomplete recovery in final acetylcholine application is from slow washout of etomidate, consistent with its membrane partitioning. Similar responses were seen from  $n = 8$  independent cells. **c** Side view of the overall cryo-EM map of the

receptor-etomidate-choline complex;  $\alpha$  subunit is in green,  $\beta$  subunit in khaki,  $\gamma$  subunit in blue,  $\delta$  subunit in violet, choline in red, etomidate in gold, cholesterol in tomato red, and phospholipids in pink; the lipid nanodisc is shown as a semi-transparent surface.  $\alpha_\gamma$  and  $\alpha_\delta$  subunits are named based on their neighboring complementary subunits. **d** Side view of two  $\alpha$  subunits showing permeation pathway as dots representing solvent-accessible surface colored by diameter; purple is 2.8–5.6 Å diameter, while diameter > 5.6 Å is shown in blue. Thr2 that forms the pore constriction is shown as sticks. **e** Etomidate-receptor interactions in  $\alpha_\gamma$  subunit are shown as sticks with corresponding density. **f** Choline at  $\alpha/\gamma$  interface.

interface, stabilizing the positively charged ammonium in an aromatic box (Fig. 1f) defined in earlier structures<sup>24,32</sup>. This compaction of loop C is part of a structural rotation and compaction of the ECD as a whole seen across the receptor superfamily<sup>33</sup>. Agonists are known to bind most tightly, at equilibrium, to the desensitized state; that etomidate stabilizes agonist binding is in line with its inhibitory activity being connected to enhancing desensitization.

The structure of the muscle-type receptor bound to etomidate and choline reveals a permeation pathway consistent with a desensitized state (Fig. 1d). The extracellular vestibule is widely open, and the transmembrane pore, comprising M2 helices from each of the five subunits, tapers from relatively wide on its extracellular end to a constriction point near the junction with the cytosol. The minimal pore diameter is 4.5 Å and is defined by threonine side chains at the 2' position, similar to what was observed in complexes with the agonists carbachol and nicotine<sup>19,20</sup>. While polar constrictions of this diameter are suggested to permit some ion passage in simulations<sup>19</sup>, this diameter is much smaller than the 7.4 Å minimum diameter estimated from ion permeability studies for an activated state<sup>34</sup>. Together, the functional and structural analyses support etomidate acting through a formerly uncharacterized intrasubunit TMD site to stabilize a non-conducting, desensitized-like channel state.

### Depolarizing blocker succinylcholine stabilizes a desensitized state

Succinylcholine is the most common neuromuscular blocker used during general anesthesia. This paralytic agent comprises two linearly linked copies of acetylcholine, with a quaternary ammonium pharmacophore on each end (Fig. 2a). It is an orthosteric agonist for the *Torpedo* nicotinic receptor and the human muscle nicotinic receptor but not the neuronal nicotinic receptors<sup>35,36</sup>. The paralytic activity of succinylcholine stems from its resistance to hydrolysis by acetylcholinesterase, which extends its lifetime in the synapse compared to the neurotransmitter, allowing it to briefly activate, then stably desensitize the receptors. Electrophysiology experiments further illustrate its low efficacy compared to acetylcholine and reveal rebound currents upon washout at high concentrations, indicative of channel block (Fig. 2a). To address questions of specificity and mechanism of action of this important anesthetic adjunct, we obtained a cryo-EM structure of the *Torpedo* nicotinic receptor in complex with succinylcholine at an overall resolution of 2.7 Å. The map quality revealed clear density for succinylcholine bound in the classical neurotransmitter sites at extracellular  $\alpha$ - $\gamma$  and  $\alpha$ - $\delta$  subunit interfaces (Fig. 2b, Supplementary Fig. 8a–c). Diffuse pore density in this structure is also consistent with the low affinity channel blocking activity (Supplementary Fig. 7).

Succinylcholine binds in a similar pose in both neurotransmitter sites, with one of its ammonium groups anchored in the classical aromatic box, while its linker and second ammonium snake away from the membrane and toward the complementary subunit. Interactions with the  $\gamma$  and  $\delta$  subunits go beyond those seen with choline and other smaller agonists and are likely responsible for the subtype selectivity of this drug versus the neuronal receptor subtypes<sup>36</sup>. Comparison of the two binding sites within the muscle-type receptor reveals a lack of conservation in complementary subunit interactions, where  $\gamma$ Y111 and  $\delta$ Y117, which interact with the second ammonium, are replaced with  $\delta$ R113 and  $\delta$ T119 (Fig. 2d, e, Supplementary Fig. 8b, c). Among these,  $\delta$ T119/ $\gamma$ Y117 stands out. In the neuronal complementary subunit  $\beta$ 2, the  $\delta$ T119/ $\gamma$ Y117 position is a phenylalanine ( $\beta$ 2F119). The substitution of threonine/tyrosine with a more hydrophobic phenylalanine may disrupt the interaction of succinylcholine with a neuronal  $\beta$ 2 subunit. The neuronal  $\beta$ 4 subunit has a leucine ( $\beta$ 4L121) at the  $\delta$ T119/ $\gamma$ Y117 position; this very

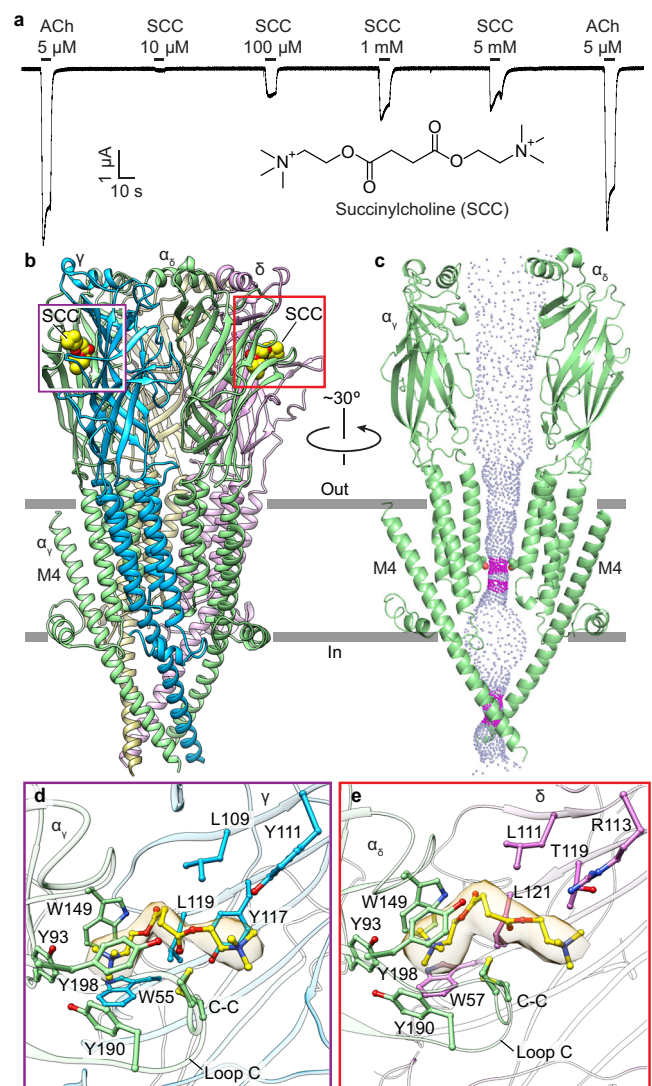


**Fig. 2 | Succinylcholine inhibition and binding mechanism.** **a** TEVC electrophysiology illustrates lower efficacy of succinylcholine (SCC) compared to acetylcholine (ACh). Similar responses were seen in  $n = 8$  independent cells. **b** Side view of succinylcholine-bound structure. Subunits are colored as in Fig. 1. Succinylcholine is shown as yellow spheres. **c** Side view of two  $\alpha$  subunits showing permeation pathway as dots representing solvent-accessible surface colored by diameter; Thr2 that forms pore constriction is shown as sticks. **d** Succinylcholine at  $\alpha/\gamma$  interface. **e** Succinylcholine at  $\alpha/\delta$  interface.

hydrophobic side chain again may disfavor interactions with succinylcholine. When the neuronal  $\alpha$ 7 subunit forms the complementary side of the binding pocket, the  $\delta$ T119/ $\gamma$ Y117 position in  $\alpha$ 7 is a glutamine ( $\alpha$ 7Q116). Superposition of the *Torpedo* receptor-succinylcholine complex with the  $\alpha$ 7 structures suggests that this glutamine would clash with the bound succinylcholine molecule and would thereby disfavor high-affinity succinylcholine binding. Furthermore, the cryo-EM map suggests that two loop C conformations are present in the  $\alpha$ <sub>v</sub> subunit: one packed down tightly as in  $\alpha$ <sub>6</sub>, and a minor more open conformation, as seen in apo and  $\alpha$ -bungarotoxin-bound structures (Supplementary Fig. 8c, d)<sup>17,19,20</sup>. Together the structural observations are consistent with different affinities for the two sites, observed with agonists like epibatidine<sup>37,38</sup> and antagonists like snake toxins<sup>39</sup> and *d*-tubocurarine<sup>40</sup>.

Binding of succinylcholine in the neurotransmitter sites coincides with the ion channel adopting a funnel-shaped conformation

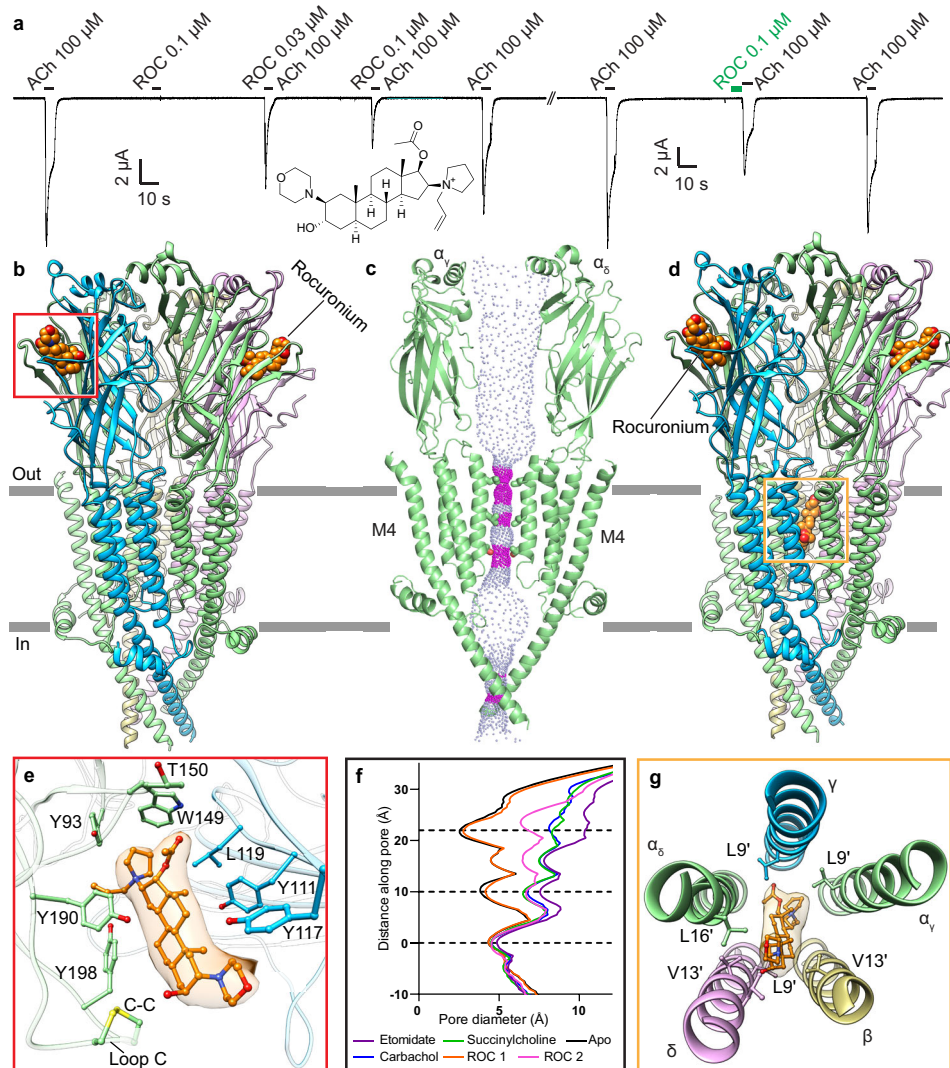


**Fig. 3 | Rocuronium inhibition and binding mechanism.** **a** TEVC recording illustrating inhibition of acetylcholine evoked currents by rocuronium (ROC, chemical structure). Second recording shows effect of rocuronium pre-application consistent with the antagonist being able to bind to the resting state. Similar responses were observed in  $n = 6$  independent cells. **b** Side view of rocuronium-bound structure, with subunits colored as in Fig. 1 and rocuronium as orange spheres. **c** Side view of two  $\alpha$  subunits showing permeation pathway of **b** as dots representing solvent-accessible surface colored by diameter. Constriction points

are formed by T244, L255 and L258, which are shown as sticks. **e** Rocuronium at  $\alpha/\delta$  interface. **d** Side view of rocuronium pore-blocked structure, with subunits colored as in Fig. 1 and rocuronium as orange spheres. **e** Rocuronium at the  $\alpha/\delta$  interface. **f** Plot of distance along pore axis vs. pore diameter for structures in this study compared to the apo receptor structure (PDB: 7SMM), ROC 1-rocuronium-bound resting-like state, ROC 2 rocuronium-bound pore-blocked state. **g** Rocuronium at pore site. Ligands and interacting residues are shown as sticks and corresponding densities of ligands are shown as semitransparent surfaces.

consistent with a desensitized state (Fig. 2c)<sup>33,41</sup>. This pore conformation is similar to that seen in the presence of etomidate. Moreover, both  $\alpha$ -M4 C-termini are detached from the receptor's coupling region in both structures (Fig. 2b, c, Supplementary Figs. 4 and 8e). The  $\beta$ ,  $\gamma$  and  $\delta$  subunits contain C-terminal extensions that interact with the receptor ECD and tether M4 in place, which may prevent their M4 helices from tilting away from the pore axis. Additionally, the movement of the  $\alpha$  subunit M4 helices likely stems from those subunits undergoing the largest conformational changes between resting and desensitized states<sup>19,20</sup>.

These findings connect the activity of agonists like succinylcholine that stabilize a desensitized state to the activity of an allosteric antagonist like etomidate that binds to the same conformation and could thereby slow recovery to a resting, activatable state. We previously found that at high concentrations, *d*-tubocurarine was bound to one of the two etomidate sites<sup>20</sup>. However, *d*-tubocurarine exerts potent antagonist activity

through binding at the classical neurotransmitter site, leading us to question whether occupancy of that allosteric site was an experimental artifact. The results with etomidate, in the context of the succinylcholine-bound receptor structure, help to support the  $\alpha$ -M4 intrasubunit site as a relevant locus for negative allosteric modulation. Together, this pair of structures suggests that in clinical anesthesia, etomidate and succinylcholine should enhance each other's muscle relaxant activities. We were curious to next contrast the mechanism of antagonism for a non-depolarizing blocker.

### Non-depolarizing blocker rocuronium stabilizes a resting-like state

Rocuronium, introduced in 1994, belongs to a newer generation of aminosteroid neuromuscular blockers and has become the paralytic of choice for rapid sequence induction of anesthesia and intubation. It is a high-affinity competitive antagonist of the muscle-type nicotinic

receptor<sup>7</sup> and inhibits acetylcholine evoked whole cell currents both when pre-applied and co-applied with agonist (Fig. 3a). Rocuronium inhibits both muscle-type and neuronal nicotinic receptors. To explore binding determinants underlying specificity of this compound, we obtained an initial cryo-EM reconstruction of the muscle-type receptor bound to rocuronium at an overall resolution of 2.8 Å (Supplementary Fig. 2b, c). Further focused classification revealed two distinct states of the receptor, one with rocuronium bound in the pore and one without (Fig. 3, Supplementary Fig. 2). Both structures contained clear density for rocuronium in both classical neurotransmitter sites (Fig. 3b, d), with loop C propped open by the ligand (Fig. 3e) and the ECD in an expanded conformation characteristic of antagonist-bound and apo Cys-loop receptors<sup>33</sup>. Rocuronium primarily makes contacts with the principal ( $\alpha_6$  and  $\alpha_V$ ) subunits in both states. On the complementary side of the neurotransmitter binding pocket, its closest interaction is with  $\gamma$ Y111 (Fig. 3e). The decreased number of interactions on the complementary subunit compared to succinylcholine may explain why rocuronium is able to bind not only muscle-type but also neuronal type receptors<sup>42</sup>. The complementary subunits are less conserved in their ligand-binding residues, and accordingly a compound that primarily interacts with the principal subunits will be more promiscuous than one that relies heavily upon interactions with the complementary binding pocket.

In the conformation with rocuronium bound only in the neurotransmitter binding sites, the receptor adopts an overall conformation like the apo resting state. The extracellular domain is more expanded than seen in the agonist-bound structures, and the channel pore contains hydrophobic constrictions in its upper half (Fig. 3c, f). This extensive hydrophobic barrier was seen in previous apo and antagonist-bound structures (Supplementary Fig. 4) and would prevent ion permeation. Also indicative of a resting-like state are the positions of the  $\alpha$ -M4 helices (Fig. 3b, Supplementary Fig. 4). In this rocuronium-bound structure, the upper position of the  $\alpha$ -M4 helices retain map density sufficient for modeling and remain in close apposition to the coupling region, contrasting with desensitized states where one or more  $\alpha$ -M4 helices are detached. Together, this first rocuronium complex shows how the non-depolarizing blocker prevents channel activation by competing with agonist, inhibits the conformational transition to an activated state, and stabilizes the pore in a resting-like nonconducting state.

In contrast, the second conformation of the rocuronium-bound receptor stabilizes a conformation intermediate between the resting and desensitized states. Density for pore blockers is typically poorly defined, as these tend to be low affinity sites, and the blocker often binds in multiple orientations. However, the density for rocuronium is remarkably clear, revealing only one possible orientation and set of interactions (Fig. 3d, g). Its binding deep in the pore causes the extracellular ends of all five M2 helices to dilate or tilt away from the channel axis (Fig. 3d, g and Supplementary Fig. 4). Breaking of the hydrophobic activation gate coincides with poorer local resolution in the extracellular ends of M2, which suggests that these helices become comparatively dynamic. The largest movement occurs in M2 of the  $\alpha_V$  subunit, which rocuronium packs against most closely (Fig. 3g). The relative widening of the upper half of the TMD pore, as seen in desensitized state structures, affects the conformation of the M4 helices as well. The M4 of the  $\alpha_V$  subunit detaches from the receptor in a manner similar to that in the carbachol-bound desensitized state, wherein only M4 of the  $\alpha_6$  subunit is detached (Supplementary Fig. 4)<sup>20</sup>. The tightest constriction in the pore is at the 2' residue T244 (Fig. 3c, f), a position also associated with the desensitized state constriction (Supplementary Fig. 4). Thus, despite the extracellular domain adopting an antagonist-bound conformation, the transmembrane domain appears to be locked in a conformation reminiscent of agonist-bound desensitized states. Could pore block contribute meaningfully to the paralytic action of rocuronium? This site is likely

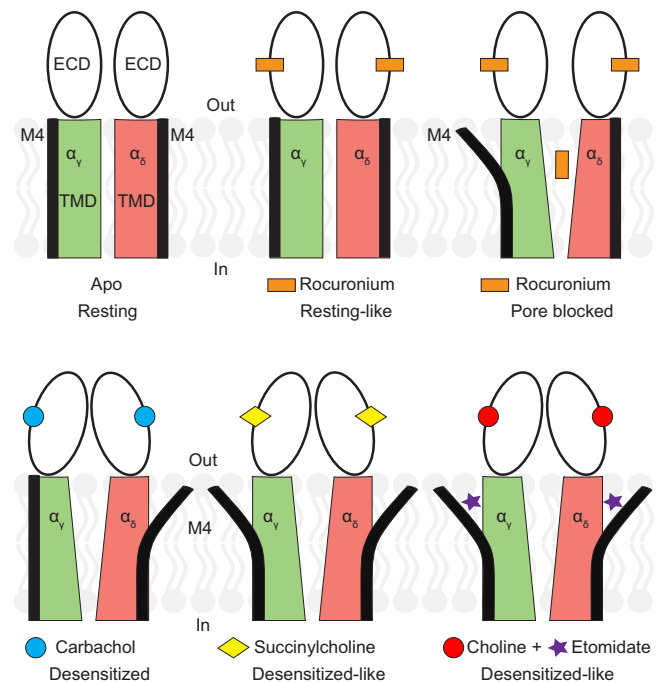


**Fig. 4 | Agonist, blocker and anesthetic receptor sites and conformational changes.** ECDs are shown as black hollow ellipses,  $\alpha_V$  subunit TMD is in green, the TMD of  $\alpha_6$  subunit is shown in red, embedded in lipid bilayer. M4 helices of both subunits are shown as thick black lines between the TMD and lipid bilayer.

too low in affinity to be relevant in a clinical setting, however the structure shows how a representative blocker binds and thereby stabilizes a unique receptor conformation where the ECD is in a resting-like state, while the TMD resembles a desensitized-like state.

## Discussion

Neuromuscular blockers paralyze skeletal muscle by antagonizing muscle nicotinic receptors; general anesthetics have also long been known to inhibit these excitatory ion channels. That these drug classes are frequently employed in combination makes it of interest to understand how they work and how they may either antagonize or enhance the other's activity. To build a foundation for understanding drug interactions, we first mapped binding interactions for representative paralytics and an anesthetic. The atomic details of receptor interactions for the paralytic agents were largely unknown. We found that the depolarizing blocker succinylcholine binds in an extended conformation at both neurotransmitter sites and stabilizes a desensitized channel state. This finding is consistent with its activity as a low efficacy agonist and its stimulation of brief muscle contractions before producing flaccid paralysis. In contrast, rocuronium, a fast-acting non-depolarizing blocker, binds to the same two receptor sites, but interacts mainly with the principal ( $\alpha$ ) subunits, and stabilizes a resting channel state. Photoaffinity experiments with etomidate analogs have proposed a wealth of sites, but which ones matter, and the effect on receptor conformational states, have been largely shrouded in mystery. We found that the intravenous anesthetic etomidate binds in a largely unpredicted site, within the TMD bundle of  $\alpha$  subunits, to stabilize a nonconducting desensitized-like state. These binding sites and correlated functional states are summarized in Fig. 4.

Emerging from these structures is an intrasubunit modulator site and mechanism for negative allosteric modulation. Previous structural studies found that in agonist bound or otherwise desensitized-like states, one or both of the  $\alpha$  subunit M4 helices are detached from the body of the receptor (Supplementary Fig. 4). This conformational change may be a component of activation that persists during

desensitization, or it may be triggered only during desensitization. In the presence of a high concentration of the desensitizing antagonist *d*-tubocurarine, this plant alkaloid can occupy one of the modulator sites, after saturating the higher affinity neurotransmitter site<sup>20</sup>. What remained unclear was whether this putative modulator site was relevant to a drug that exerted its principal activity through that site. The current study suggests that etomidate is an example of this drug class. The structures suggest that any ligand whose binding results in M4 detachment, and opening up of this modulator site, would enhance the inhibitory activity of etomidate; further, etomidate would enhance the tendency of an agonist to desensitize the receptor. Non-depolarizing blockers like rocuronium, in contrast, should allosterically inhibit etomidate binding; put another way, etomidate should increase the effective dose of rocuronium needed to compete off acetylcholine. Consequences in the clinic are likely unsubstantial for this case, as both ligands would still act to antagonize channel activity, and rocuronium is a much more potent antagonist than etomidate. Together, these structural studies provide a foundation for understanding the muscle relaxant effects of a representative intravenous anesthetic and how it may interact with commonly used neuromuscular blockers.

## Methods

### Receptor purification

Nicotinic acetylcholine receptor protein was purified from the electric organ of *T. californica* (EastCoast Bio) as previously described<sup>15,17</sup>. Briefly, 100 g of frozen tissue were thawed in 300 mL of buffer A (20 mM NaH<sub>2</sub>PO<sub>4</sub>, 400 mM NaCl, pH 7.4) supplemented with 150 mg NEM (N-ethylmaleimide, Sigma). Thawed tissue was homogenized and centrifuged at 3220 × *g* for 15 min. The supernatant was passed through cheesecloth and a protease inhibitor tablet (cOmplete mini, Sigma) was added to it with gentle stirring. Cell membranes were pelleted by centrifuging this supernatant at 105,000 × *g* for 30 min. The membrane pellet was collected and resuspended in buffer B (20 mM Tris, 80 mM NaCl, 1 mM EDTA, 20% sucrose, pH 11.0) and incubated on ice for 30 min. The resuspension was centrifuged at 105,000 × *g* for 30 min. The membrane pellet was washed twice with buffer C (20 mM NaH<sub>2</sub>PO<sub>4</sub>, 80 mM NaCl, pH 7.4) and stored at −80 °C until further use. For protein purification, 2 g of the membrane pellet were thawed on ice. A homogenizer (Dounce) was used to resuspend the pellet in 50 mL of buffer C. Triton X-100 (1.5% v/v) and phenylmethylsulfonyl fluoride (PMSF, 1 mM) were added to the sample, which was gently rocked for 1 h at 4 °C. The solubilized supernatant was collected by centrifuging the sample at 105,000 *g* for 30 min at 4 °C. 100 mL of buffer C were added to the supernatant. The affinity reagent ATM (2-[(4-aminobutanoyl)amino]-*N,N,N*-trimethylethanaminium) was coupled to NHS activated Sepharose resin (Cytiva) as reported previously<sup>15,17</sup>. Affinity resin (5 mL packed bed) was equilibrated with buffer C and mixed with diluted supernatant. The suspension was nutated for 1 h at 4 °C. Unbound sample was removed by washing the resin with buffer D (20 mM Tris, 80 mM NaCl, 1 mM EDTA, 1 mM *n*-dodecyl-β-D-maltoside, DDM, Anatrace, pH 7.4). For preparation of the receptor-succinylcholine sample, we used buffer E (20 mM Tris, 80 mM NaCl, 1 mM EDTA, 1 mM DDM, 50 mM βME, pH 7.4) containing 50 mM succinylcholine for elution. To prepare the rocuronium and etomidate samples, we used 1.2 M choline chloride (Sigma) as the eluting agent followed by the addition of respective ligands after elution (200 μM for both). Fluorescence size exclusion chromatography was used to analyze the quality of the elution fractions by monitoring tryptophan fluorescence. The eluted sample was concentrated to A<sub>280</sub> = 7–8 using Amicon Ultra concentrators (Millipore) with a 100 kDa molecular weight cutoff.

### Reconstitution of protein into lipid nanodiscs

The sample was reconstituted into lipidic nanodiscs composed of soy polar lipids (Avanti Polar Lipids) and saposin. A molar ratio of receptor:

saposin: soy polar lipids of 1:25:150 was used. Saposin A expression plasmid was kindly provided by Salipro Biotech<sup>43</sup>. For the rocuronium sample, cholesterol was added to the lipids in a ratio of 1:4. Briefly, the concentrated receptor was mixed with the lipid suspension and incubated at RT for 20 minutes, after which saposin was added. The reaction mix was incubated at RT for another 2 min. One hundred milligrams of Bio-Beads (SM-2 Bio-Rad) were washed once with methanol and three times with Milli-Q water and once with TBS (20 mM Tris, 80 mM NaCl, pH 7.4). Five hundred microliters of sample and washed biobeads were mixed and rotated overnight at 4 °C. Freshly washed Bio-Beads were replaced in the reaction tube and rotated for another 1–2 h. The reconstituted sample was aspirated using a 1 mL syringe and needle and ultracentrifuged at 98,600 × *g* for 30 min to remove precipitate or Bio-Beads. The sample was then passed through a Superose 6 10/300 GL Increase (Cytiva) column equilibrated with TBS to isolate the pentameric receptor species by removing empty nanodiscs and protein aggregates.

### Cryo-EM sample preparation

To obtain the succinylcholine-bound structure, 1 mM succinylcholine chloride (Sigma) was added to the TBS used in SEC. To obtain the rocuronium-bound structure, SEC elution fractions of apo receptor were supplemented with 200 μM rocuronium bromide (Tokyo Chemical Industry) both before and after concentrating. To obtain the etomidate and choline bound structure, 200 μM of etomidate (Tocris) was added only to SEC fractions. All samples were concentrated to an A<sub>280</sub> of 7–8 and centrifuged at 98,600 × *g* to remove aggregates. Freshly prepared fluorinated Fos-Choline-8 (Anatrace) was added to the final sample at a concentration of 0.5 mM to induce random orientations of the protein molecules. 3 μL of sample were applied to Quantifoil R 1.2/1.3 (200 mesh, Copper) grids and plunge frozen in liquid ethane using a Vitrobot Mark IV (FEI).

### Cryo-EM data collection and processing

Cryo-EM grids were screened on the Talos Arctica at UT Southwestern Medical Center. Cryo-EM datasets were collected on 300 kV Titan Krios microscopes (FEI) at the PNCC (see Supplementary Table 1). Dose-fractionated micrographs were processed following a general RELION 3.1<sup>44</sup> workflow. Structural biology software was compiled by SBGrid<sup>45</sup>. Pseudosymmetry did not pose problems during particle alignment, as described previously<sup>20</sup>. Movies were gain normalized, 2x Fourier binned, dose weighted, aligned and summed using MotionCor2<sup>46</sup>. Defocus values were estimated with GCTF<sup>47</sup>. CTF corrected particles were picked using cryOLO<sup>48</sup>. Good particles were selected using 2D classification. 2D classes with good structural features were used to generate a de novo initial model for 3D classification. Particles from 3D classes with strong intracellular domain (ICD) density were selected for further 3D refinement. The particles were polished, followed by a round of CTF refinement. A final 3D refinement and sharpening were performed. Focused classification after signal subtraction was used to resolve heterogeneity in the rocuronium sample. For the signal subtraction, a mask around the α<sub>y</sub> subunit was used.

### Model building, refinement and validation

The *d*-tubocurarine bound structure of the *Torpedo* receptor (PDB: 7SMR) was used as a starting model for succinylcholine and etomidate plus choline bound structures. The chemical structures of succinylcholine, etomidate, and choline were adapted from the PDB ligand repository. The apo structure of the *Torpedo* receptor (PDB ID: 7SMM) was used as a starting model for the rocuronium-bound structure. The geometry restraints for rocuronium were generated using the Grade Web Server (<http://grade.globalphasing.org>). Manual building and local refinement were performed in Coot<sup>49</sup> and global real space refinement was performed in Phenix<sup>50</sup>. Stereochemistry and clashes were assessed using Phenix and the Molprobity<sup>51</sup> server. Analysis of the



ion pore was done using HOLE<sup>52</sup>. UCSF Chimera<sup>53</sup>, ChimeraX<sup>54</sup> and Pymol (Schrodinger, LLC) were used to generate map and model figures.

### Electrophysiology

Open reading frames of the *Torpedo*  $\alpha$ ,  $\beta$ ,  $\gamma$  and  $\delta$  subunit-coding genes were subcloned into the pGHI9 vector. The genes were kindly provided by Dr. Steven Sine from the Mayo Clinic. cRNAs were prepared from subcloned constructs using MEGascript T7 Transcription kit (Thermo Fisher). *Xenopus laevis* ovary lobes were purchased from the National Xenopus Resource Center and maintained in Barth's solution (in mM: 88 NaCl, 1 KCl, 2.4 NaHCO<sub>3</sub>, 0.82 MgSO<sub>4</sub>, 0.33 Ca(NO<sub>3</sub>)<sub>2</sub>, 0.68 CaCl<sub>2</sub>, 10 HEPES, pH 7.4) supplemented with 25  $\mu$ g/mL ampicillin and 10  $\mu$ g/mL gentamycin at 16 °C. Ovarian lobes were cut into small pieces and washed with Barth's solution. Cut lobes were digested with 1 mg/mL Type-I Collagenase (Gibco) in Barth's solution supplemented with 1 mg/mL bovine serum albumin for 45–60 min. Digested ovarian lobes were shaken in 130 mM potassium hydrogen phosphate buffer, pH 6.5 (titrated by mixing monobasic and dibasic salts) for 15 min to facilitate release of oocytes from the lobes. Isolated oocytes were washed with ND96 solution (in mM: 96 NaCl, 2 KCl, 1 MgCl<sub>2</sub>, 1.8 CaCl<sub>2</sub>, and 5 HEPES pH 7.4) and analyzed under a microscope. Stage V-VI oocytes were isolated and stored in ND96 solution supplemented with 25  $\mu$ g/mL ampicillin and 10  $\mu$ g/mL gentamycin. Oocytes were micro-injected with 0.1–5 ng cRNA mixture of the subunits in the ratio 2:1:1 of  $\alpha$ : $\beta$ : $\gamma$ : $\delta$ . Microinjections were performed in ND96 solution prepared without calcium. Approximately 24–72 h after injection, TEVC recordings were performed using an Axoclamp 900 A (Molecular Devices) amplifier and a Digidata 1550B (Molecular Devices) digitizer. Pipettes were polished to a resistance of 0.2–1.2 M $\Omega$  and filled with filtered 1 M KCl solution. ND96 was used as the bath solution and carrier of ligands. Data were analyzed using pClamp 10.7 (Molecular Devices).

### Reporting summary

Further information on research design is available in the Nature Portfolio Reporting Summary linked to this article.

### Data availability

The data that support this study are available from the corresponding authors upon request. Cryo-EM maps have been deposited in the Electron Microscopy Data Bank (EMDB) under accession codes [EMD-28576](#) (rocuronium-bound resting-like state), [EMD-28826](#) (rocuronium pore-blocked state), [EMD-28892](#) (etomidate-bound desensitized-like state) and [EMD-28893](#) (succinylcholine-bound desensitized-like state). Atomic model coordinates have been deposited in the Protein Data Bank (PDB) under accession code [8ESK](#) (rocuronium-bound resting-like state), [8F2S](#) (rocuronium pore-blocked state), [8F6Y](#) (etomidate-bound desensitized-like state), and [8F6Z](#) (succinylcholine-bound desensitized-like state). We have used the following published structures for comparison with our data: [6X3V](#), [7SMM](#), [7QKO](#), [6UWZ](#), [7Z14](#), [7SMR](#), [7QL6](#), [7QL5](#), [7SMS](#). Source data are provided with this paper.

### References

- Butterworth Iv, J. F., Mackey, D. C. & Wasnick, J. D. *Morgan & Mikhail's Clinical Anesthesiology* 6th edn (McGraw-Hill Education, 2018).
- Krasowski, M. D. & Harrison, N. L. General anaesthetic actions on ligand-gated ion channels. *Cell Mol. Life Sci.* **55**, 1278–1303 (1999).
- Franks, N. P. & Lieb, W. R. Molecular and cellular mechanisms of general anaesthesia. *Nature* **367**, 607–614 (1994).
- Forman, S. A., Chiara, D. C. & Miller, K. W. Anaesthetics target interfacial transmembrane sites in nicotinic acetylcholine receptors. *Neuropharmacology* **96**, 169–177 (2015).
- Rudolph, U. & Antkowiak, B. Molecular and neuronal substrates for general anaesthetics. *Nat. Rev. Neurosci.* **5**, 709–720 (2004).
- Kopp Lugli, A., Yost, C. S. & Kindler, C. H. Anaesthetic mechanisms: update on the challenge of unravelling the mystery of anaesthesia. *Eur. J. Anaesthesiol.* **26**, 807–820 (2009).
- Miller, R. D. & Gropper, M. A. *Miller's Anesthesia* 9th edn, 667 (Elsevier, 2020).
- Forman, S. A. Combining mutations and electrophysiology to map anesthetic sites on ligand-gated ion channels. *Methods Enzymol.* **602**, 369–389 (2018).
- Violet, J. M., Downie, D. L., Nakisa, R. C., Lieb, W. R. & Franks, N. P. Differential sensitivities of mammalian neuronal and muscle nicotinic acetylcholine receptors to general anaesthetics. *Anesthesiology* **86**, 866–874 (1997).
- Wachtel, R. E. & Wegrzynowicz, E. S. Kinetics of nicotinic acetylcholine ion channels in the presence of intravenous anaesthetics and induction agents. *Br. J. Pharmacol.* **106**, 623–627 (1992).
- Husain, S. S. et al. p-Trifluoromethyl diazirinyl-etomidate: a potent photoreactive general anesthetic derivative of etomidate that is selective for ligand-gated cationic ion channels. *J. Med. Chem.* **53**, 6432–6444 (2010).
- Donati, F. & Bevan, D. R. Potentiation of succinylcholine phase II block with isoflurane. *Anesthesiology* **58**, 552–555 (1983).
- Hashmi, N. K., McCartney, S., Jones, L. H. & Bartz, R. R. in *Cardiac Intensive Care* 3rd edn (ed Brown, D. L.) 525–547.e522 (Elsevier, 2019).
- Evans, F. T., Gray, P. W., Lehmann, H. & Silk, E. Sensitivity to succinylcholine in relation to serum-cholinesterase. *Lancet* **1**, 1229–1230 (1952).
- Rahman, M. M., Worrell, B. T., Stowell, M. H. B. & Hibbs, R. E. *Methods in Enzymology*, Vol. 653. 189–206 (Academic Press, 2021).
- Unwin, N. Refined structure of the nicotinic acetylcholine receptor at 4 Å resolution. *J. Mol. Biol.* **346**, 967–989 (2005).
- Rahman, M. M. et al. Structure of the native muscle-type nicotinic receptor and inhibition by snake venom toxins. *Neuron* **106**, 952–962.e955 (2020).
- Nys, M. et al. The molecular mechanism of snake short-chain alpha-neurotoxin binding to muscle-type nicotinic acetylcholine receptors. *Nat. Commun.* **13**, 4543 (2022).
- Zarkadas, E. et al. Conformational transitions and ligand-binding to a muscle-type nicotinic acetylcholine receptor. *Neuron* **110**, 1358–1370.e1355 (2022).
- Rahman, M. M. et al. Structural mechanism of muscle nicotinic receptor desensitization and block by curare. *Nat. Struct. Mol. Biol.* <https://doi.org/10.1038/s41594-022-00737-3> (2022).
- Schindler, H. & Quast, U. Functional acetylcholine receptor from *Torpedo marmorata* in planar membranes. *Proc. Natl Acad. Sci. USA* **77**, 3052–3056 (1980).
- Dowding, A. J. & Hall, Z. W. Monoclonal antibodies specific for each of the two toxin-binding sites of *Torpedo* acetylcholine receptor. *Biochemistry* **26**, 6372–6381 (1987).
- Chiara, D. C. et al. Time-resolved photolabeling of the nicotinic acetylcholine receptor by [3H]azietomidate, an open-state inhibitor. *Mol. Pharmacol.* **75**, 1084–1095 (2009).
- Karlin, A. Emerging structure of the nicotinic acetylcholine receptors. *Nat. Rev. Neurosci.* **3**, 102–114 (2002).
- Noda, M. et al. Structural homology of *Torpedo californica* acetylcholine receptor subunits. *Nature* **302**, 528–532 (1983).
- Raftery, M. A., Hunkapiller, M. W., Strader, C. D. & Hood, L. E. Acetylcholine receptor: complex of homologous subunits. *Science* **208**, 1454–1456 (1980).
- Hamouda, A. K., Stewart, D. S., Husain, S. S. & Cohen, J. B. Multiple transmembrane binding sites for p-trifluoromethyl diazirinyl-etomidate, a photoreactive *Torpedo* nicotinic acetylcholine receptor allosteric inhibitor. *J. Biol. Chem.* **286**, 20466–20477 (2011).
- Husain, S. S. et al. 2-(3-Methyl-3H-diaziren-3-yl)ethyl 1-(1-phenylethyl)-1H-imidazole-5-carboxylate: a derivative of the

- stereoselective general anesthetic etomidate for photolabeling ligand-gated ion channels. *J. Med. Chem.* **46**, 1257–1265 (2003).
29. Ziebell, M. R., Nirthanan, S., Husain, S. S., Miller, K. W. & Cohen, J. B. Identification of binding sites in the nicotinic acetylcholine receptor for [<sup>3</sup>H]azietomidate, a photoactivatable general anesthetic. *J. Biol. Chem.* **279**, 17640–17649 (2004).
  30. Nirthanan, S., Garcia, G. 3rd, Chiara, D. C., Husain, S. S. & Cohen, J. B. Identification of binding sites in the nicotinic acetylcholine receptor for TDBzl-etomidate, a photoreactive positive allosteric effector. *J. Biol. Chem.* **283**, 22051–22062 (2008).
  31. Kim, J. J. et al. Shared structural mechanisms of general anaesthetics and benzodiazepines. *Nature* **585**, 303–308 (2020).
  32. Gharpure, A., Noviello, C. M. & Hibbs, R. E. Progress in nicotinic receptor structural biology. *Neuropharmacology* **171**, 108086 (2020).
  33. Nemezc, A., Prevost, M. S., Menny, A. & Corringier, P. J. Emerging molecular mechanisms of signal transduction in pentameric ligand-gated ion channels. *Neuron* **90**, 452–470 (2016).
  34. Dwyer, T. M., Adams, D. J. & Hille, B. The permeability of the end-plate channel to organic cations in frog muscle. *J. Gen. Physiol.* **75**, 469–492 (1980).
  35. Bowman, W. C. *Pharmacology of Neuromuscular Function* 2nd edn (Wright, 1990).
  36. Jonsson, M. et al. Activation and inhibition of human muscular and neuronal nicotinic acetylcholine receptors by succinylcholine. *Anesthesiology* **104**, 724–733 (2006).
  37. Prince, R. J. & Sine, S. M. Epibatidine binds with unique site and state selectivity to muscle nicotinic acetylcholine receptors. *J. Biol. Chem.* **273**, 7843–7849 (1998).
  38. Pennington, R. A., Gao, F., Sine, S. M. & Prince, R. J. Structural basis for epibatidine selectivity at desensitized nicotinic receptors. *Mol. Pharmacol.* **67**, 123–131 (2005).
  39. Osaka, H., Malany, S., Kanter, J. R., Sine, S. M. & Taylor, P. Subunit interface selectivity of the alpha-neurotoxins for the nicotinic acetylcholine receptor. *J. Biol. Chem.* **274**, 9581–9586 (1999).
  40. Neubig, R. R. & Cohen, J. B. Equilibrium binding of [<sup>3</sup>H]tubocurarine and [<sup>3</sup>H]acetylcholine by Torpedo postsynaptic membranes: stoichiometry and ligand interactions. *Biochemistry* **18**, 5464–5475 (1979).
  41. Gielen, M. & Corringier, P. J. The dual-gate model for pentameric ligand-gated ion channels activation and desensitization. *J. Physiol.* **596**, 1873–1902 (2018).
  42. Jonsson, M. et al. Distinct pharmacologic properties of neuromuscular blocking agents on human neuronal nicotinic acetylcholine receptors: a possible explanation for the train-of-four fade. *Anesthesiology* **105**, 521–533 (2006).
  43. Frauenfeld, J. et al. A saposin-lipoprotein nanoparticle system for membrane proteins. *Nat. Methods* **13**, 345–351 (2016).
  44. Zivanov, J. et al. New tools for automated high-resolution cryo-EM structure determination in RELION-3. *Elife* **7** <https://doi.org/10.7554/eLife.42166> (2018).
  45. Morin, A. et al. Collaboration gets the most out of software. *Elife* **2**, e01456 (2013).
  46. Zheng, S. Q. et al. MotionCor2: anisotropic correction of beam-induced motion for improved cryo-electron microscopy. *Nat. Methods* **14**, 331–332 (2017).
  47. Zhang, K. Gctf: Real-time CTF determination and correction. *J. Struct. Biol.* **193**, 1–12 (2016).
  48. Wagner, T. et al. SPHIRE-crYOLO is a fast and accurate fully automated particle picker for cryo-EM. *Commun. Biol.* **2**, 218 (2019).
  49. Emsley, P., Lohkamp, B., Scott, W. G. & Cowtan, K. Features and development of Coot. *Acta Crystallogr D. Biol. Crystallogr* **66**, 486–501 (2010).
  50. Afonine, P. V. et al. Real-space refinement in PHENIX for cryo-EM and crystallography. *Acta Crystallogr D. Struct. Biol.* **74**, 531–544 (2018).
  51. Williams, C. J. et al. MolProbity: More and better reference data for improved all-atom structure validation. *Protein Sci.* **27**, 293–315 (2018).
  52. Smart, O. S., Neduveilil, J. G., Wang, X., Wallace, B. A. & Sansom, M. S. HOLE: a program for the analysis of the pore dimensions of ion channel structural models. *J. Mol. Graph* **14**, 354–360, 376 (1996).
  53. Pettersen, E. F. et al. UCSF Chimera—a visualization system for exploratory research and analysis. *J. Comput. Chem.* **25**, 1605–1612 (2004).
  54. Pettersen, E. F. et al. UCSF ChimeraX: structure visualization for researchers, educators, and developers. *Protein Sci.* **30**, 70–82 (2021).

## Acknowledgements

We thank L. Baxter for assistance with illustrations, C. Noviello for assistance in cryo-EM sample screening, and M. Stowell, J. Cohen, S. Burke, W. Chojnacka, and C. Noviello for critical manuscript feedback. We thank M. Stowell and B. Worrell for generously providing the ATM affinity reagent. Single-particle cryo-EM grids were screened at the University of Texas Southwestern Medical Center Cryo-Electron Microscopy Facility, which is supported by the CPRIT Core Facility Support Award RP170644. We thank the PNCC for cryo-EM data collection under user proposals 50839 and 51574, supported by NIH grant U24GM129547 and performed at the PNCC at OHSU and accessed through EMSL (grid.436923.9), a DOE Office of Science User Facility sponsored by the Office of Biological and Environmental Research. U.G. and M.M.R. acknowledge predoctoral and postdoctoral fellowships from the American Heart Association (82735, 827474). This work was supported by grants from the NIH to REH (NS120496, DAO42072).

## Author contributions

U.G. performed the sample preparation and data processing for cryo-EM, model building and validation, structural analysis, and drafted the manuscript with R.E.H. J.T. and U.G. performed the electrophysiology. M.M.R. assisted in structural analysis, model building and validation, and preparation of figures. U.G. and R.E.H. revised the manuscript with input from all other authors.

## Competing interests

The authors declare no competing interests.

## Additional information

**Supplementary information** The online version contains supplementary material available at <https://doi.org/10.1038/s41467-023-38827-5>.

**Correspondence** and requests for materials should be addressed to Ryan E. Hibbs.

**Peer review information** *Nature Communications* thanks the anonymous reviewers for their contribution to the peer review of this work. A peer review file is available.

**Reprints and permissions information** is available at <http://www.nature.com/reprints>

**Publisher's note** Springer Nature remains neutral with regard to jurisdictional claims in published maps and institutional affiliations.

**Open Access** This article is licensed under a Creative Commons Attribution 4.0 International License, which permits use, sharing, adaptation, distribution and reproduction in any medium or format, as long as you give appropriate credit to the original author(s) and the source, provide a link to the Creative Commons license, and indicate if changes were made. The images or other third party material in this article are included in the article's Creative Commons license, unless indicated otherwise in a credit line to the material. If material is not included in the article's Creative Commons license and your intended use is not permitted by statutory regulation or exceeds the permitted use, you will need to obtain permission directly from the copyright holder. To view a copy of this license, visit <http://creativecommons.org/licenses/by/4.0/>.

© The Author(s) 2023